

# LIBRE: The Multiple 3D LiDAR Dataset

Alexander Carballo<sup>1,4</sup> Jacob Lambert<sup>2,4</sup> Abraham Monrroy<sup>2,4</sup> David Wong<sup>1,4</sup> Patiphon Narksri<sup>2,4</sup>  
Yuki Kitsukawa<sup>2,4</sup> Eijiro Takeuchi<sup>2,4</sup> Shinpei Kato<sup>3,4,5</sup> Kazuya Takeda<sup>1,2,4</sup>

**Abstract**—In this work, we present LIBRE: LiDAR Benchmarking and Reference, a first-of-its-kind dataset featuring 12 different LiDAR sensors, covering a range of manufacturers, models, and laser configurations. Data captured independently from each sensor includes four different environments and configurations: static obstacles placed at known distances and measured from a fixed position within a controlled environment; static obstacles measured from a moving vehicle, captured in a weather chamber where LiDARs were exposed to different conditions (fog, rain, strong light); dynamic objects actively measured from a fixed position by multiple LiDARs mounted side-by-side simultaneously, creating indirect interference conditions; and dynamic traffic objects captured from a vehicle driven on public urban roads multiple times at different times of the day, including data from supporting sensors such as cameras, infrared imaging, and odometry devices. LIBRE will contribute the research community to (1) provide a means for a fair comparison of currently available LiDARs, and (2) facilitate the improvement of existing self-driving vehicles and robotics-related software, in terms of development and tuning of LiDAR-based perception algorithms.

**Index Terms**—3D LiDAR, dataset, adverse weather, indirect interference, range accuracy, pointcloud density, LIBRE

## I. INTRODUCTION

LiDARs (*Light Detection And Ranging*, sometimes *Light Imaging Detection And Ranging* for the image-like resolution of modern 3D sensors) are one of the core perception technologies which have shaped the field of Advanced Driver Assistance System (ADAS) and autonomous driving vehicles. While LiDARs are relative newcomers to the automotive industry when compared with radars and cameras, 2D and especially 3D LiDARs have demonstrated high measurement accuracy and illumination independent sensing capabilities for self-driving tasks[1]. Of course, not only automotive applications, LiDARs have been deployed in wheeled autonomous robots, drones, humanoid robots, consumer level applications, and at intersections in smart cities. The rapid development of research and industry relating to self-driving

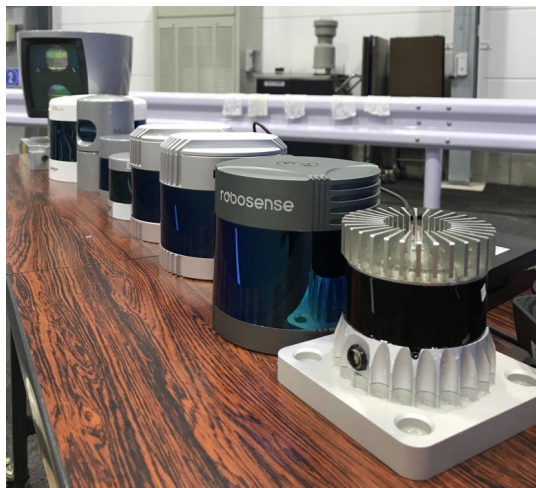


Fig. 1: Multiple 3D LiDARs

vehicles has created a large demand for such sensors. Depending on the individual perception application and operating domain, there are several key LiDAR performance attributes: measurement range, measurement accuracy, point density, scan speed and configurability, wavelength, robustness to environmental changes, form factor, and cost. As such, a large number of LiDAR manufacturers have emerged in recent years introducing new technologies to address such needs[2].

With many different manufacturers and technologies becoming available, it is necessary to assess the perception characteristics of each device according to the intended application. In addition, while each LiDAR manufacturer subject their products to quality tests (vibration and shock endurance, tolerance to electromagnetic interference (EMI), water and dust ingress protection (IP), operating temperature and pressure, measurement accuracy for different reflectors, etc.), LiDARs are meant for general use and not exclusively tested on vehicles. Furthermore, with LiDAR costs remaining high, it can be difficult to select the best LiDAR in terms of cost performance for a particular application. In this study, we aim to collect data to enable the attribute analysis of several 3D LiDARs for applications in autonomous driving vehicles. We capture data to evaluate LiDARs in terms of: measurement range, accuracy, density, object detection, mapping and localization, and robustness to weather conditions and interference. During our study we collected a large dataset of vehicle-mounted LiDARs both in normal traffic scenes, and in a controlled chamber for testing performance

<sup>1</sup>Institute of Innovation for Future Society, Nagoya University, Furo-cho, Chikusa-ku, Nagoya 464-8601, Japan.

<sup>2</sup>Graduate School of Informatics, Nagoya University, Furo-cho, Chikusa-ku, Nagoya 464-8603, Japan.

<sup>3</sup>Graduate School of Information Science and Technology, University of Tokyo, 7-3-1 Hongo, Bunkyo-ku, Tokyo, 113-0033, Japan.

<sup>4</sup>TierIV Inc., Nagoya University Open Innovation Center, 1-3, Mei-eki 1-chome, Nakamura-Ward, Nagoya, 450-6610, Japan.

<sup>5</sup>The Autoware Foundation, 3-22-5, Hongo, Bunkyo-ku, Tokyo, 113-0033, Japan. Email: alexander@g.sp.m.is.nagoya-u.ac.jp, jacob.lambert@g.sp.m.is.nagoya-u.ac.jp, abraham.monrroy@tier4.jp, david.wong@tier4.jp, narksri.patiphon@g.sp.m.is.nagoya-u.ac.jp, yuki.kitsukawa@tier4.jp, takeuchi@g.sp.m.is.nagoya-u.ac.jp, shinpei@is.s.u-tokyo.ac.jp, kazuya.takeda@nagoya-u.jp

Dataset	LiDAR(s)	Image	Labels	Diversity	Other sensors, notes
Stanford Track Collection[3]	1 (HDL-64S2)	-	3D	E	GPS/IMU
KITTI[4]	1 (HDL-64)	Yes	2D/3D	E	3x Cam (Stereo), GPS/IMU
KAIST multispectral[5]	1 (HDL-32E)	Yes	2D/3D	E/T	2 Cameras, 1 Thermal (infrared) cam. IMU+GNSS
nuScenes[6]	1 (HDL-32E)	Yes	2D/3D	E/T/W	6 Cameras, 5 RADARs, GNSS, IMU
H3D[7]	1 (HDL-64S2)	Yes	2D/3D	E	3 Cameras, IMU+GNSS
ApolloScape[8]	2 (2x Riegl VUX-1HA)	Yes	2D/3D	E/T/W	Depth Images, GPS/IMU,
LiVi-Set[9]	2 (HDL-32E, VLP-16 <sup>a</sup> )	Yes	-	E	Dash-board camera, CAN (driving behavior dataset)
ArgoVerse[10]	2 (2x VLP-32C)	Yes	2D/3D	E	7 Cameras ring, 2 Stereo cams, GNSS
FORD Campus[11]	3 (HDL-64S2, 2x Riegl LMS-Q120)	Yes	-	E	Camera, 360° cam., IMU, INS
Oxford RobotCar[12]	3 (2x SICK LMS-151 (2D), SICK LD-MRS (3D))	Yes	-	E/T/W	3x Cameras, Stereo cam., GPS
Waymo[13]	5 (1 360° 75m range, 4x "HoneyComb" 20m range <sup>b</sup> )	Yes	2D/3D	E/T/W	5 Cameras
<b>LIBRE (ours)</b>	12 (VLS-128 <sup>1</sup> , HDL-64S2, HDL-32E, VLP-32C, VLP-16, Pandar-64, Pandar-40p, OS1-64, OS1-16, RS-Lidar32, C32, C16)	Yes	2D/3D <sup>2</sup>	E/T/W	Camera, IMU, GNSS, CAN, 360° 4K cam., Event cam., Infrared cam., 3D pointcloud map, Vector map

TABLE I: Publicly available datasets featuring LiDARs (arranged chronologically and by number of LiDARs, names of LiDAR manufacturers are omitted for those models in this study). Diversity refers to changes in the data collected, as in types of environments (E), times of day (T), weather conditions (W). <sup>a</sup>The authors in [9] state they only used the HDL-32E. <sup>b</sup>LiDARs proprietary and developed by Google/Waymo.

in adverse weather conditions. To leverage with the above limitations, we released the LIBRE dataset covering multiple 3D LiDARs.<sup>3</sup> It features 12 LiDARs, each one a different model from diverse manufacturers. Fig. 1 shows some of the 3D LiDARs used in our evaluations. LIBRE dataset includes data from four different environments and configurations:

- *Dynamic traffic*: dynamic traffic objects (vehicles, pedestrians, bicycles, buildings, etc.) captured from a vehicle driving on public urban roads around Nagoya University
- *Static targets*: static objects (reflective targets, black car and a mannequin), placed at known controlled distances, and measured from a fixed position
- *Adverse weather*: static objects placed at a fix location and measured from a moving vehicle while exposing the LiDARs to adverse conditions (fog, rain, strong light)
- *Indirect interference*: dynamic traffic objects measured from a fixed position by multiple LiDARs simultaneously and exposed to indirect interference conditions

The contributions of this work are summarized as follows. We introduce the LIBRE dataset including data from 12 different LiDARs in the above environments and configurations. We present a quantitative summary of performance of the different LiDARs in terms of range and density for static targets, and a qualitative evaluation of response to adverse weather conditions. We also provide a qualitative evaluation of object detection under indirect interference conditions. While this paper offers some limited analysis of the large amount of data captured, the main contribution is the publishment of a novel and openly available dataset

<sup>1</sup>In addition to the VLS-128, the Velodyne Alpha Prime will be also added to the dataset.

<sup>2</sup>At the time of writing, 2D/3D data labeling is ongoing. Labels will be included for a subsets of the dynamic traffic data.

<sup>3</sup>A teaser of LIBRE dataset was released in January 28th, 2020 at <https://sites.google.com/g.sp.m.is.nagoya-u.ac.jp/libre-dataset>. The full set will be released during 2020.

which will allow many researchers to perform more detailed analysis and comparisons.

This paper is structured as follows: Section II presents related datasets featuring LiDARs, while Section III describes our dataset. Section IV presents results on dynamic traffic scenes, Section V static evaluations, Section VI weather chamber tests, and Section VII detection in presence of interference. Finally, this paper is concluded in Section VIII.

## II. LIDAR DATASETS

Table I summarizes current datasets featuring LiDARs, and highlights the contributions made by our dataset. The Stanford Track Collection[3] carefully records tracks of objects and their dataset offer the object tracks, while FORD Campus vision and LiDAR dataset[11] include several complete scenes captured by multiple LiDARs. The Oxford RobotCar Dataset[12] has one 3D LiDAR and two 2D LiDARs, and accumulation of 2D data as the vehicle moves allows the reconstruction of 3D scenes. ApolloScape[8] features two 3D LiDARs, in several environments, times of the day and varying weather. The KAIST dataset[5] features 3D LiDAR (905 nm infrared) plus normal vision and a thermal (long wave infrared 8  $\mu\text{m}$  to 15  $\mu\text{m}$ ), and is therefore considered multispectral. The Lidar-video driving dataset[9] also collects data from one LiDAR, a camera and CAN bus data targeting driving behaviour.

More recently, the ArgoVerse dataset[10] features two LiDARs —one on top of the other, plus a ring of cameras for 360° annotation. Vector maps (HD maps) are also provided. The nuScenes dataset by Aptiv[6] features one LiDAR, several cameras and other sensors, and is captured in a diverse range of environments, times of day and weather conditions. The Honda Research Institute 3D (H3D)[7] also features one LiDAR and multiple sensors, with labels provided at 2 Hz and propagated at 10 Hz so as to provide labels at the same rate as the LiDAR. The Waymo Open Dataset[13] features 5













	Velodyne					Hesai		Ouster		RoboSense	LeiShen	
												
	VLS-128	HDL-64S2	HDL-32E	VLP-32C	VLP-16	Pandar-64	Pandar-40p	OS1-64	OS1-16	RS-Lidar32	C32-151A	C16-700B
Channels	128	64	32	32	16	64	40	64	16	32	32	16
FPS[Hz]	5-20	5-20	5-20	5-20	5-20	10,20	10,20	10,20	10,20	5,10,20	5,10,20	5,10,20
Precision[m]	$\pm 0.03$	$\pm 0.02^a$	$\pm 0.02$	$\pm 0.03$	$\pm 0.03$	$\pm 0.02^c$	$\pm 0.02^c$	$\pm 0.03^d$	$\pm 0.03^d$	$\pm 0.03^c$	$\pm 0.02$	$\pm 0.02$
Max.Range[m]	245	120	100	200	100	200	200	120	120	200	150	70
Min.Range[m]		3	2	1	1	0.3	0.3	0.8	0.8	0.4	0.5	0.5
vFOV[deg]	40	26.9	41.33	40	30	40	40 33.2	33.2	40	32	30	30
vRes[deg]	0.11 <sup>b</sup>	0.33 <sup>a</sup>	1.33	0.33 <sup>b</sup>	2.0	0.167 <sup>b</sup>	0.33 <sup>b</sup>	0.53	0.53	0.33 <sup>b</sup>	1	2
$\lambda$ [nm]	903	903	903	903	903	905	905	850	850	905	905	905
$\phi$ [mm]	165.5	223.5	85.3	103	103.3	116	116	85	85	114	120	102
Weight(kg)	3.5	13.5	1.0	0.925	0.830	1.52	1.52	0.425	0.425	1.17	1.5	0.87

TABLE II: LiDARs tested in this study, by manufacturer and number of channels (rings). Acronyms are frame rate (FPS), vertical field-of-view (vFOV), vertical resolution (vRes), laser wavelength ( $\lambda$ ), and diameter  $\phi$ . <sup>a</sup>Velodyne states HDL-64S2 accuracy is  $\pm 2m$  for 80% of channels, and  $\pm 5m$  for the remaining; vRes for  $+2^\circ \dots -8.33^\circ$  is  $1/3^\circ$  and for  $-8.83^\circ \dots -24.33^\circ$  is  $1/2^\circ$ . <sup>b</sup>Minimum (or finest) resolution, as these sensors have variable angle difference between beams. <sup>c</sup>Hesai and RoboSense state that accuracy for  $0.3m \dots 0.5m$  is  $\pm 0.05m$ , then  $\pm 0.02m$  from  $0.5m \dots 200m$ . <sup>d</sup>Ouster states accuracy for  $0.8m \dots 2m$  is  $\pm 0.03m$ , for  $2m \dots 20m$  is  $\pm 0.015m$ , for  $20m \dots 60m$  is  $\pm 0.03m$ , and over  $60m$  is  $\pm 0.10m$ . <sup>4</sup>

LiDARs created by Google/Waymo, one  $360^\circ$  and 4 for lower FOV and proximity detection in several different locations.

Different from the above works, this would be the first dataset to collect data under the similar conditions but with different LiDARs. Some of the above datasets feature more than one LiDAR but with limited models, while in our work we offer 12 different models. Also, as far as we know, no static tests of LiDARs are publicly available, nor is any other publicly available evaluation with multiple LiDARs of different types active at the same time in the same environment.

Besides datasets featuring LiDARs, other related works have consider diverse LiDAR evaluations. Jokela *et al.*[14] tested 5 different LiDARs in fog and rain conditions at Clermont-Ferrand’s 31 m long fog chamber[15], including different perception targets and conditions; they also evaluated these LiDARs under low temperature snowy environments. While our present study lacks evaluations under snowy conditions, we test a broader range of sensors in a wider variety of adverse weather experiments.

### III. LIBRE DATASET

LIBRE dataset features 5 LiDARs from Velodyne Lidar<sup>5</sup>, two from Ouster Inc.<sup>6</sup>, two from Hesai Photonics Technology Co., Ltd<sup>7</sup>, one from RoboSense–Suteng Innovation Technology Co., Ltd.<sup>8</sup>, and two from Leishen Intelligent Systems Co., Ltd.<sup>9</sup>. Table II describes the general specifications of each tested device.

<sup>4</sup>Sensor images are not to scale and copyrights are owned by their respective manufacturers.

<sup>5</sup><https://velodynelidar.com>

<sup>6</sup><https://ouster.com>

<sup>7</sup><https://www.hesaitech.com>

<sup>8</sup><http://www.robosense.ai>

<sup>9</sup><http://www.leishen-lidar.com>

All these sensors correspond to the multi-beam (multi-channel) mechanical scanning type: several pairs of laser diodes and photo-detectors (avalanche photo detector (APD) and single-photon avalanche diode (SPAD)) and corresponding emit-remit optics and mirrors, are rotated by a motor for  $360^\circ$  which defines azimuth, while the vertical angle of a laser and photo-detector pair defines elevation. All sensors in this selection have short-wave infrared (SWIR) wavelengths between 850 nm, 903 nm and 905 nm. While some support multiple returns (echoes), the data collected in our dataset always records only the strongest echo.

## IV. DYNAMIC DATA

### A. Data Collection

The target was to collect data in a variety of traffic conditions, including different type of environments, varying density of traffic and times of the day. We drove our instrumented vehicle (Fig. 2) three times per day and collected data for the following key time periods:

- Morning (9am-10am)
- Noon (12pm-1pm)
- Afternoon (2pm-4pm)

Fig. 3 shows the vehicle used for data capture. The 3D LiDAR on top was replaced for each experiment only after the three time periods were recorded, only one LiDAR was used at a time to avoid noise due to mutual interference. Data from other sensors (RGB camera, IR camera,  $360^\circ$  camera, event camera, IMU, GNSS, CAN) was also recorded together with LiDAR data, together with timestamps, using ROS[16]. In addition, we collected calibration data for each new LiDAR setup to perform extrinsic LiDAR to camera calibration, using a checkerboard and various other points of interest. Clear lighting conditions were ensured to record such data.

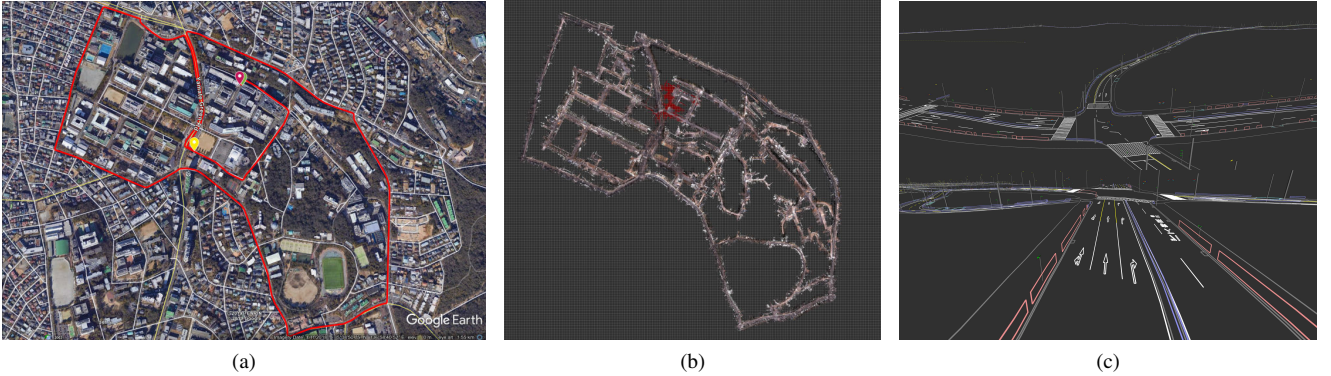


Fig. 2: Map of the dynamic environment included in the dataset: (a) location reference, ● and ● markers denote the starting and goal points, respectively, ● corresponds to a vehicle gate in/out the campus, and ● corresponds the location of the indirect interference experiment. (b) is the pointcloud map (grid cell size 10 m) and (c) some scenes with the vector map.



Fig. 3: Instrumented vehicle used to capture static and dynamic data

The routes driven in this data capture also have a reference pointcloud map available, which was created by a professional mobile mapping system (MMS). This map includes RGB data, and vector map files (HD map) for public road outside of the Nagoya University campus, and is also provided as part of the dynamic traffic data.

### B. Evaluation in Autoware

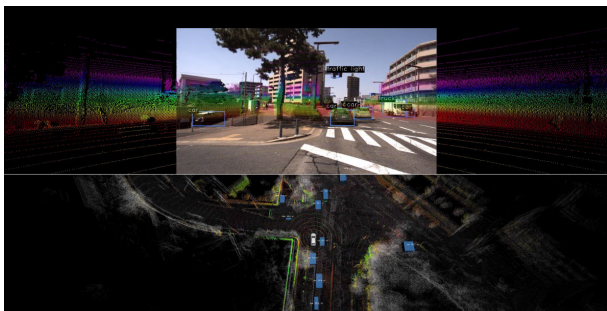


Fig. 4: Dynamic traffic scenes by applying SOTA algorithms on pointcloud.

Fig. 4 shows qualitative results of running state-of-the-art algorithms, implemented in the self-driving open source

platform Autoware<sup>10</sup> (see Kato *et al.*[17]), on LiDAR pointclouds. Fig. 4 shows VLS-128 pointcloud when localized using the Normal Distributions Transform (NDT), LiDAR/camera fusion, and CNN-based object detection.

### V. STATIC TARGETS

For the static targets and the adverse weather conditions, we used the Japan Automobile Research Institute (JARI<sup>11</sup>) weather experimental facilities. Fig. 5(a) shows a cross view of such facilities during our experiments. It is a 200 m long indoor weather chamber with 3 straight and marked lanes (each 3.5 wide as per Japanese regulations), regularly flat, with fences, traffic lights, controlled illumination and ventilation, multiple sprinklers for fog and rain. Description of JARI's weather chamber equipment and conditions are given in Section VI.

As shown on Fig. 5(c), the static targets in this study include: A0 size reflective targets (Edmund Optics light absorbing black-out black velvet sheet (10% reflectance), polyboard white, and 3M diamond-grade 4090 series sheet), a Toyota Esquire black mini-van, two mannequins wearing black clothes, and occasionally human participants when conditions were safe.

During this experiment, each LiDAR was warmed up for at least 30 min to increase detection accuracy of the photo-detectors. As shown in Fig. 5(d), we used a Leica Geosystems Total Station Viva TS15[18] and reflector prisms to setup the ground truth for target positions. Table III shows the target distances (along the LiDAR's  $x$ -axis) and the actual measured distances with the TS15. Reflective targets were carefully aligned at each measurement position, which we previously marked on the road surface, while the mini-van and the mannequins were approximately aligned with this. Fig. 5(b) shows the 5 m mark as an example.

We used two metrics to compare LiDARs measurement performance: range accuracy and density. We segmented the reflective targets as a whole and individually. We accumulated 40 frames of LiDAR data and rejected data with

<sup>10</sup><https://gitlab.com/autowarefoundation/autoware.ai>

<sup>11</sup><http://www.jari.or.jp>

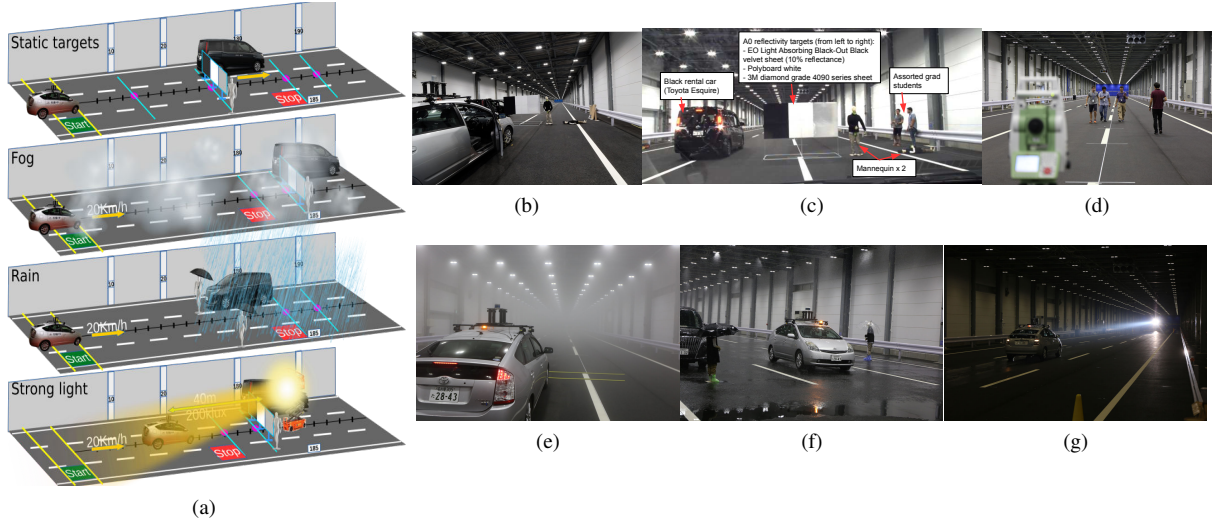


Fig. 5: Static targets and adverse weather experiments at JARI's weather chamber: (a) configuration of the different scenarios, (b) and (c) measurement, (e) to (g) sample adverse weather scenes, (d) setting up ground truth.

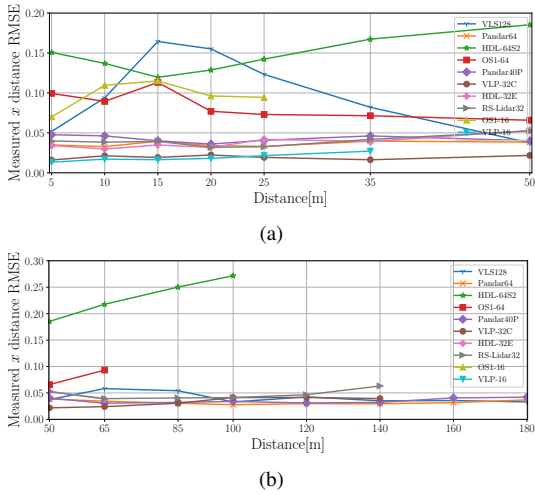


Fig. 6: Range RMSE on  $x$ -axis distance per LiDAR, (a) short to mid range, and (b) mid to long range.

insufficient points (min. 5 points per target). RMSE between the measured points and the ground truth was calculated at every distance, and a summary is shown in Figs. 6(a) for 0m to 50m range and 6(b) for 50m to 180m range. We can easily see that generally, RMSE grows with distance and some LiDARs struggle at very close distances. Upon closer investigation, some LiDARs specifically struggle with high reflectivity targets at close range.

Fig. 7 shows the actual number of points detected on the reflective targets, averaged over 40 frames, 7(a) for 0m to 50m range and 7(b) for 50m to 180m range, respectively. Even though the VLS-128 has double the number of channels, the Pandar64 has the higher density at all distances, and Pandar40P follows closely the density of VLS-128. The RS-Lidar32 has better density than the VLP-32C and HDL-32E at the same number of channels. The OS1-16 comparatively low density at each distance, and the OS1-64 drops very rapidly within the first 20m and after 35m provides a similar

Distance to Lidar [m]	Target Ground Truth [m]	Distance to Lidar [m]	Target Ground Truth [m]
5	4.982	60	65.008
10	9.998	85	85.005
15	14.994	100	100.010
20	20.001	120	120.006
25	25.999	140	140.005
35	35.007	160	160.007
50	49.997	180	180.007

TABLE III: Target distances and LiDAR to targets ground truth, as measured by the TS15.

density to the sensors with a lower number of channels.

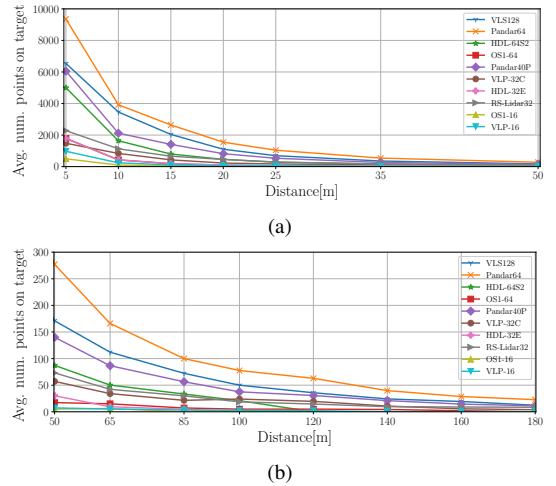


Fig. 7: Average density (number of points) on target per LiDAR, (a) short to mid range, and (b) mid to long range.

## VI. ADVERSE WEATHER

JARI's weather experimental facilities allowed us to test LiDARs in controlled weather conditions (refer to Fig. 5(a)). For fog emission, this weather chamber has  $7.5 \mu\text{m}$  particle size and controllable visibility of 10m up to 80m, with fog emitted over the complete 200m track. For rain emission,

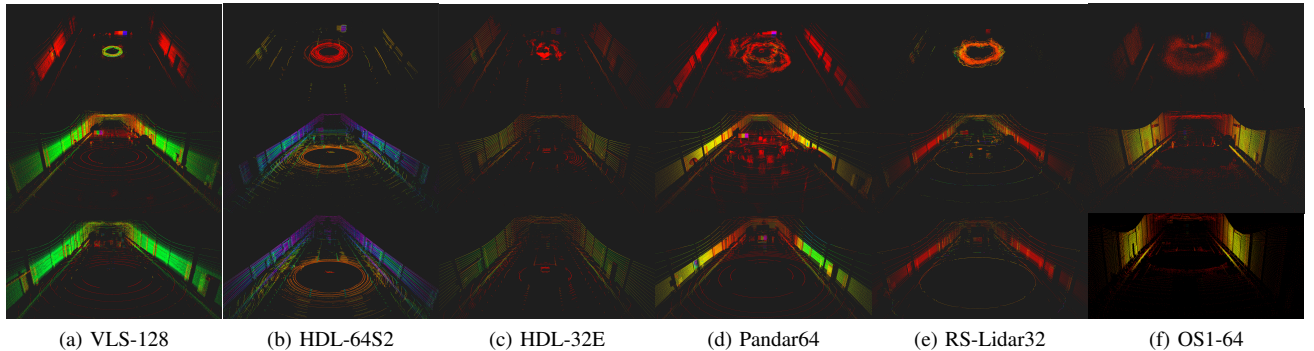


Fig. 8: Adverse weather results, color represents intensity, top row: fog, middle row: rain, and bottom row: strong light.

there are two different sprinklers with particle size of  $640\ \mu\text{m}$  and  $1400\ \mu\text{m}$ , and 3 precipitation levels: strong (30 mm/h), intense (50 mm/h), and very intense (80 mm/h). In our study we used strong and very intense. Rain is emitted only for half of the track (100 m). Strong “sun” light comes from a controlled mobile 6 kW xenon light source with maximum luminous intensity of 350 Mcd, adjustable position, yaw and pitch angles. It has an optional yellow filter to approximate the color temperature of the sun; however, as it reduces illuminance, we tested without this filter for a maximum color temperature of 6000 K (sample scene in Fig. 5(g)). In our experiment, the maximum illuminance at the LiDAR mount position on the car was set to 200 klx (full sunlight illuminance at noon) at a distance of 40 m from the light source. This means illuminance gradually increases from the starting position, reaching the peak illuminance at 40 m from the light source, and then decreases towards the stopping position.

For safety reasons, during the adverse weather experiments, we drove the vehicle between 15 km/h and 25 km/h. Due to poor visibility during fog and light experiments, we also added small bumps on the road (see Fig. 5(e)) so the driver could identify the slow down and stopping positions; as we drove forward and backwards, there were two such stopping areas at either end of the track. For all the weather experiments, a passenger was present to lend an extra pair of eyes to the driver. The driver, other team members and the JARI staff kept constant communication over push-talk radios to regulate the start and end of each run, and to ensure safety. For the fog experiment, we ensured fog density before each experiment. For the strong light experiment, both driver and passenger and other people outside the vehicle wore special dark sunglasses. The strong light experiment was conducted right after the rain experiment, thus our data has the additional value of including specular reflections (Fig. 5(f)) due to the wet road surface for half the test track. We also recorded RGB camera and IR camera data during these experiments.

The fog experiment started with a very dense 10 m visibility and the vehicle drove forward towards the stop position, then backwards towards the start position, waited 30 s for the fog to dissipate, and repeated again until perceived visibility was over 80 m. As it takes about 10 min for the fog chamber

to reach maximum density again, so during this time we changed LiDARs (we kept other LiDARs warming up at least 30 min before any test) and repeated. For the rain experiment, we started with a 30 mm/h precipitation rate, waited about 1 min for it to become steady, and drove the vehicle backwards towards the stop position and then forward to the start position only one time; as rain falls only in the last half of the track, our vehicle made transitions from dry to rainy and vice versa, with targets inside the rainy area. We then set the 80 mm/h precipitation rate and repeated driving, returning to the start position to change LiDARs for the next test. Finally, the strong light experiment happened after rain experiment therefore half the test track was wet creating specular reflection conditions; from the start position we turned on the xenon light source, drive forward towards the stop position (passing through the maximum illuminance zone) and backwards towards the start position, turned off the light, changed the LiDAR, and repeated.

Adverse weather qualitative results are shown on Fig. 8 for a selection of LiDARs. The top row shows the fog experiment when the vehicle was close to the targets, the middle row shows the rain experiment at 30 mm/h precipitation rate with the vehicle under the rainy area, and the bottom row shows the strong light experiment when the vehicle was close to the highest illuminance area. All LiDARs were affected in a similar way by fog: several of the low reflection intensity points tend to form a toroidal shape around the LiDAR for the echo from the fog is stronger, the highly reflective walls are partially visible but with a much lower intensity values, with only the highly reflective white markers in the road and the diamond-grade and white reflectors ahead are partially visible with a diminished intensity; this means that much of the intensity of the reflected light is scattered and attenuated by the fog. Rain also affects all the LiDARs: while it does not attenuate reflections, it creates fake obstacles especially when precipitation rate is high and non uniform. This situation is clearly shown in Figs. 8(a), (d) and (e). The rain experiment was not encouraging, as most LiDARs detected the water showers from the sprinklers as vertical pillars, as shown in Fig. 9. This points to the need of better rain generation systems in weather chambers.

Finally, during the strong light experiment, when the vehicle was approximately at the maximum illuminance area,

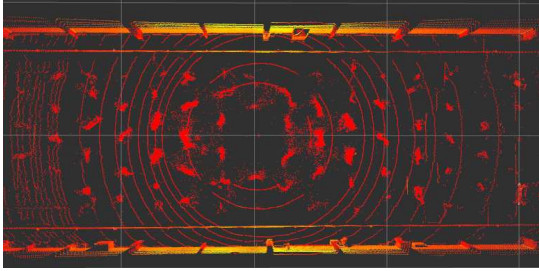


Fig. 9: “Rain pillars” as detected by a LiDAR.

we obtained almost no data from the experiment targets, road and back wall in front of the LiDAR. These elements become again visible when the vehicle is in other areas with much lower illuminance. While such strong illuminance is not expected at the horizon, certain LiDAR setups on the car, especially when LiDARs are mounted with large roll/pitch angles, will be affected by strong sunlight.



Fig. 10: LiDARs layout for the indirect interference test at Nagoya University campus.

## VII. INDIRECT INTERFERENCE

Indirect interference refers to the situation where light of one sensor (A) reflects from a target and is received at a different sensor (B), and sensor B’s azimuthal angle of scanning is aligned with this incoming reflection. If the azimuthal angle of scanning is slightly different, the received light may not converge through the remission optics into the photo-detection (APD or SPAD).

For our indirect interference experiment, we selected a 340m long mostly-flat road at Nagoya University (see Fig. 2(a)). The road is used by pedestrians, cyclists and vehicles moving around the campus. In addition we used a calibration board obstacle from close to far distance to test interference and intensity patterns. Fig. 10 shows the layout of sensors for this experiment. A cardboard separator was added in between LiDARs to avoid mutual (direct) interference. All sensors were warmed up for over 30 min to ensure higher accuracy at the APD. Results of having all LiDARs simultaneously scanning the scene and indirectly interfering each other are presented in Fig. 11 (for a selection of LiDARs). The upper row shows situations, in particular the highlighted rectangular area, with relatively low interference noise, middle row shows strong interference “fringe” patterns, and the bottom row highlights those interference areas.

All sensors rotate with same frequency (10Hz) but without any option for phase-locked synchronization, spinning directions (CW and CCW) are different, current azimuth

angle of laser emission cannot be controlled (each sensor takes a different time to achieve stable scanner rotation), and the sequence of laser firing at each channel is also different, therefore, it is hard to model the occurrence of interference. However, its effects on the pointcloud are easier to identify. Some sensors (VLS-128 and HDL-64S2) show curve-like fringe patterns, others (HDL-32E and Pandar40P) show conical fringes, and others very random interference noise. The most seriously affected, in terms of the area of interference noise, was the OS1-64 despite its very different wavelength. While these are qualitative results, they clearly show how indirect interference is affecting sensors.

## VIII. CONCLUSIONS

In this work we introduced an unprecedented collection of data from multiple 3D LiDARs, made publicly available for research and industry, with the objective of improving our understanding of the capabilities and limitations of popular LiDARs for autonomous vehicles. This dataset will enable benchmarking of new LiDARs, better representations in vehicle simulation software, direct comparison of LiDARs capabilities before purchasing, and better perception algorithms.

This study still lacks some important conditions such as low temperature snowy environments, night time scenes, direct interference, realistic rain, other wavelengths, and so on, which will be addressed in future extensions. However, this work sheds light onto existing issues with LiDARs which require research: the serious noise induced by indirect interference and strong light, the almost null visibility during dense fog, and the need for adequate existing object detection algorithms to work with multiple LiDARs.

This dataset will be extended by adding more sensors, environments, and other evaluations, including new perception open-source software, and coming publications. We are preparing a second phase which will include, among others, newer solid-state LiDARs (MEMS-based scanners), different wavelengths such as 1550 nm, and other scanning techniques.

## ACKNOWLEDGMENTS

We would like to extend our gratitude to the Japan Automobile Research Institute (JARI) for all the support while using their JTOWN weather chamber and other facilities. We appreciate the help of the Autoware Foundation<sup>12</sup> to realize this project. Finally, and as a matter of course, this work would not have been possible without the invaluable support of Velodyne Lidar, Ouster Inc., Hesai Photonics Technology Co., Ltd., RoboSense–Suteng Innovation Technology Co., Ltd., and Leishen Intelligent Systems Co., Ltd.

## REFERENCES

- [1] S. Thrun, M. Montemerlo, H. Dahlkamp, D. Stavens, A. Aron, J. Diebel, P. Fong, J. Gale, M. Halpenny, G. Hoffmann *et al.*, “Stanley: The robot that won the DARPA Grand Challenge,” *Journal of Field Robotics*, vol. 23, no. 9, pp. 661–692, 2006.

<sup>12</sup><https://www.autoware.org>

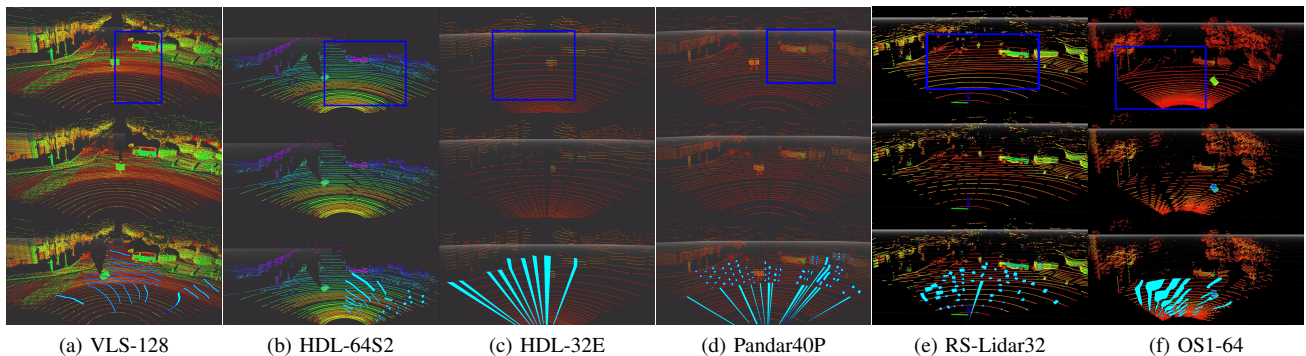


Fig. 11: Indirect interference results, highly affected areas in the road surface (“fringe-like” patterns) are highlighted.

- [2] Yole Développement. The automotive LiDAR market. [http://www.woodsdecap.com/wp-content/uploads/2018/04/Yole\\_WCP-LiDAR-Report\\_April-2018-FINAL.pdf](http://www.woodsdecap.com/wp-content/uploads/2018/04/Yole_WCP-LiDAR-Report_April-2018-FINAL.pdf). [Accessed 10-January-2020].
- [3] A. Teichman, J. Levinson, and S. Thrun, “Towards 3d object recognition via classification of arbitrary object tracks,” in *IEEE International Conference on Robotics and Automation (ICRA)*. IEEE, 2011, pp. 4034–4041.
- [4] A. Geiger, P. Lenz, C. Stiller, and R. Urtasun, “Vision meets robotics: The KITTI dataset,” *International Journal of Robotics Research (IJRR)*, 2013.
- [5] Y. Choi, N. Kim, S. Hwang, K. Park, J. S. Yoon, K. An, and I. S. Kweon, “KAIST multi-spectral day/night data set for autonomous and assisted driving,” *IEEE Transactions on Intelligent Transportation Systems*, vol. 19, no. 3, pp. 934–948, 2018.
- [6] H. Caesar, V. Bankiti, A. H. Lang, S. Vora, V. E. Liong, Q. Xu, A. Krishnan, Y. Pan, G. Baldan, and O. Beijbom, “nuScenes: A multimodal dataset for autonomous driving,” *arXiv preprint arXiv:1903.11027*, 2019.
- [7] A. Patil, S. Malla, H. Gang, and Y.-T. Chen, “The H3D dataset for full-surround 3d multi-object detection and tracking in crowded urban scenes,” in *IEEE International Conference on Robotics and Automation (ICRA)*, 2019.
- [8] X. Huang, X. Cheng, Q. Geng, B. Cao, D. Zhou, P. Wang, Y. Lin, and R. Yang, “The ApolloScape dataset for autonomous driving,” in *Proceedings of the IEEE Conference on Computer Vision and Pattern Recognition Workshops*, 2018, pp. 954–960.
- [9] Y. Chen, J. Wang, J. Li, C. Lu, Z. Luo, H. Xue, and C. Wang, “Lidar-video driving dataset: Learning driving policies effectively,” in *Proceedings of the IEEE Conference on Computer Vision and Pattern Recognition*, 2018, pp. 5870–5878.
- [10] M.-F. Chang, J. W. Lambert, P. Sangkloy, J. Singh, S. Bak, A. Hartnett, D. Wang, P. Carr, S. Lucey, D. Ramanan, and J. Hays, “Argoverse: 3d tracking and forecasting with rich maps,” in *Conference on Computer Vision and Pattern Recognition (CVPR)*, 2019.
- [11] G. Pandey, J. R. McBride, and R. M. Eustice, “Ford campus vision and lidar data set,” *The International Journal of Robotics Research*, vol. 30, no. 13, pp. 1543–1552, 2011.
- [12] W. Maddern, G. Pascoe, C. Linegar, and P. Newman, “1 Year, 1000km: The Oxford RobotCar Dataset,” *The International Journal of Robotics Research (IJRR)*, vol. 36, no. 1, pp. 3–15, 2017.
- [13] P. Sun, H. Kretschmar, X. Dotiwalla, A. Chouard, V. Patnaik, P. Tsui, J. Guo, Y. Zhou, Y. Chai, B. Caine, V. Vasudevan, W. Han, J. Ngiam, H. Zhao, A. Timofeev, S. Ettinger, M. Krivokon, A. Gao, A. Joshi, Y. Zhang, J. Shlens, Z. Chen, and D. Anguelov, “Scalability in perception for autonomous driving: Waymo open dataset,” *arXiv preprint arXiv:1912.04838*, 2019.
- [14] M. Jokela, M. Kuttila, and P. Pyykönen, “Testing and validation of automotive point-cloud sensors in adverse weather conditions,” *Applied Sciences*, vol. 9, no. 11, p. 2341, 2019.
- [15] M. Colomb, K. Hirech, P. André, J. Boreux, P. Lacote, and J. Dufour, “An innovative artificial fog production device improved in the european project fog,” *Atmospheric Research*, vol. 87, no. 3–4, pp. 242–251, 2008.
- [16] M. Quigley, B. Gerkey, K. Conley, J. Faust, T. Foote, J. Leibs, E. Berger, R. Wheeler, and A. Ng, “ROS: an open-source robot operating system,” in *IEEE International Conference on Robotics and Automation (ICRA) Workshop on Open Source Robotics*, Kobe, Japan, May 2009.
- [17] S. Kato, S. Tokunaga, Y. Maruyama, S. Maeda, M. Hirabayashi, Y. Kitsukawa, A. Monroy, T. Ando, Y. Fujii, and T. Azumi, “Autoware on board: Enabling autonomous vehicles with embedded systems,” in *ACM/IEEE International Conference on Cyber-Physical Systems (ICCP)*. IEEE, 2018, pp. 287–296.
- [18] Leica Geosystems AG. Leica Viva TS15 Datasheet. <http://w3.leica-geosystems.com/downloads/123/zz/tps/viva%20ts15/brochures-datasheet/leica%20viva%20ts15%20datasheet.us.pdf>. [Accessed 29-January-2020].